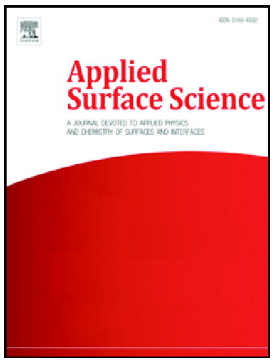

Nanoengineered nickel/reduced graphene oxide composites: Control of interfacial nanostructure for tunable electrophysical properties

Maryam Salimian, Maxim S. Ivanov, Igor Bdikin, Darius Pohl, Steffen Oswald, Vladimir A. Khomchenko, José António Paixão, Bernd Rellinghaus, Paula A.A.P. Marques, Gil Gonçalves

PII: S0169-4332(19)32597-8

DOI: https://doi.org/10.1016/j.apsusc.2019.143781

Reference: APSUSC 143781

To appear in: *Applied Surface Science*

Received date: 20 May 2019

Revised date: 2 August 2019

Accepted date: 23 August 2019

Please cite this article as: M. Salimian, M.S. Ivanov, I. Bdikin, et al., Nanoengineered nickel/reduced graphene oxide composites: Control of interfacial nanostructure for tunable electrophysical properties, *Applied Surface Science*(2019), https://doi.org/10.1016/j.apsusc.2019.143781

Nanoengineered Nickel/reduced graphene oxide composites: control of interfacial nanostructure for tunable electrophysical properties

Maryam Salimian,[1] Maxim S. Ivanov,[2] Igor Bdikin,[1] Darius Pohl,[3] Steffen Oswald,[3] Vladimir A. Khomchenko,[2] José António Paixão,[2] Bernd Rellinghaus,[3] Paula A. A. P. Marques[1] and Gil Gonçalves*[1]*

[1]TEMA-NRD, Mechanical Engineering Department, University of Aveiro, P-3810-193 Aveiro, Portugal

[2]CFisUC, Department of Physics, University of Coimbra, P-3004-516 Coimbra, Portugal

[3]IFW Dresden, Institute for Metallic Materials, P.O. Box 270116, D-01171, Dresden, Germany

*Corresponding authors. E-mail: ggoncalves@ua.pt (Gil Gonçalves)

Keywords: nickel/graphene nanocomposites, solvothermal method, electrical properties, Kelvin probe force microscopy, local current distribution

Abstract

Here we present a novel solvothermal synthesis approach for the accurate control over the structural features of nickel/reduced graphene oxide (Ni/rGO) nanocomposites for tuneable electrical properties. We discovered that the dynamic chemical structure of GO during reaction, acts as an active template for the controlled nanostructured growth of nickel nanoparticles (Ni NPs). Therefore, the precise control of reaction time offered the possibility to modulate nucleation and coalescence phenomena of Ni NPs, allowing in this way to precisely adjust their size, density and NiO@Ni structure on the final Ni/rGO nanocomposites. The electrophysical properties (work function and conductivity) of different Ni/rGO nanocomposites were determined and found to be directly dependent on the Ni NPs radius and also on the NiO buffer layer width. We confirmed a crucial role of the NiO buffer layer thickness at the Pt-NiO-Ni-NiO-rGO interface changing the conductivity from metallic to those specific to a Schottky contact or to a p-n heterojunction. These new findings reveal a relevant potential for using Ni/rGO nanocomposites as a versatile and promising material for micro-, nano- and optoelectronics as well as for energy storage technologies.

1. Introduction

Graphene oxide (GO) has been widely explored as a fundamental building block in the architecture of novel nanocomposites with high performance in different areas of application.[1] The high active surface area, light weight, large thermal stability and electrical conductivity are remarkable features that make graphene-related material extraordinary substrates.[2-4] Additionally, GO exhibits important chemical features for the controlled nanostructured growth of NPs.[5] Indeed, the intimate integration between GO and NPs can generate interesting synergies for nanoelectronics,[6] biomedical,[7] energy storage,[8] catalysis,[9] chemical and biological sensor[10] applications.

The remarkable magnetic,[11] conductive,[12] catalytic[13] and hydrogen storage[14] properties of Nickel (Ni) NPs highlight their potential for the incorporation into graphene-related materials for development of new multifunctional nanocomposites.[15] Recently, Tian et al. [16] reported a one-step production of Ni/rGO nanocomposites using ethylene glycol as a solvent and poly(N-vinyl-2-pyrrolidone) as a stabilizer. The authors observed the formation of spherical Ni NPs with an average size of 8 nm, well distributed on rGO surface, able to provide excellent catalytic properties.[16] Unprecedented work performed by Li et al. described the preparation of carbon monoliths evenly decorated with superfine Ni NPs through the formation of covalent bonds with carbon (Ni-C). After thermal treatment, the nanocomposite showed a very uniform dispersion of isolated Ni NPs with an average size of 10 nm and a very narrow size distribution.[17]

Notably, GO offers the possibility to tailor its surface chemically in order to modulate the growth of Ni NPs for engineering novel nanostructured materials. A novel approach for the synthesis of Ni/graphene nanocomposites using pre-doped graphene with sulphur and nitrogen (N-S-G) for the functionalization with hybrid Ni tetrapyridyloxyphthalocyanine (NiTPPc) via solvothermal method was recently reported by Zhang et al.[18] The results

showed that the establishment of π-π interactions allows a homogenous coverage of the N-S-G surface with the NiTPPc nanocrystals with an average size of around 10 nm. The nanocomposite exhibited superior electrocatalytic activity towards the oxidation of bisphenol A, comparing with pristine NiTPPc or N-S-G. Recently, amine functionalized GO showed a higher appetency for the incorporation of the nickel-Schiff base. The resultant nanocomposites showed multifunctional behavior, with significant improvements in mechanical, thermal and electroconductive properties.[19]

Ni-based nanocomposites require some concerns with respect to their synthesis. The ability of Ni NPs to be spontaneously oxidized can impair its final functionality. In fact, the development of feasible synthetic methodologies for the accurate control over the structural features of Ni/NiO core/shell NPs in nanocomposites at environmental conditions remains a huge challenge. A very effective approach consists on the nanoconfinement of Ni NPs in a carbon shell that provides the control of Ni core size, optimization of electronic structure and protection against chemical corrosion.[20] Yuan et al. reported a new methodology for the fabrication of Ni NPs with an average size of 23 nm, encapsulated in few-layer nitrogen-doped graphene for high-performance electromagnetic wave absorbing material.[21] However, the reported synthetic process of the nanocomposites required several steps, including carbonization at high temperature (900°C) and subsequent treatment in hot acid solution. Recently, Patange et al. [22] showed that the surface passivation by thermal treatment of the Ni/NiO core/shell NPs with graphitic carbon layer played a critical role for their stabilization under air environment. In addition, they provided relevant evidences that NiO/Ni structural features of NPs are directly correlated with their final magnetic and electrical properties.[22]

This work reports a new and efficient methodology for the synthesis of different nanostructured NiO@Ni/rGO nanocomposites for fine-tuning their final electrical

properties. Here, GO was explored as an active template for the controlled growth and preservation of nanostructured Ni/NiO NPs. We observed that the chemical metamorphosis of GO at different reaction stages obtained by reduction during solvothermal treatment can mediate the Ni NPs size and distribution and more importantly stabilize their Ni/NiO core/shell nanostructure under environmental conditions. Notably, this work provides the experimental evidences of theoretical results previously obtained by Cheng et al., dedicated to the first-principle calculation of electronic structure of the graphene/metal oxide interfaces.[23] In particular, the Schottky barrier height (SBH) and the Schottky-Mott limit (SML) were calculated for the graphene/Ni/NiO-Ni interface which is similar to that investigated in this current work for the Ni/rGO nanocomposites. Moreover, we provide a comparison of theoretical and experimental values for the SBH, SML and work function (WF) being consistent with the theoretical predictions described.[6, 23] The decrease of conductivity and increase of WF were observed with increasing Ni NPs radius and NiO buffer layer width. Importantly, the electrophysical properties of the different nanocomposites were preserved over the time under environmental conditions. Previously, we reported a new methodology for the controlled synthesis of the GO/Ni nanocomposites.[24] In this case, although significant morphological changes of Ni NPs were attained, the electrical properties of rGO/Ni nanocomposites containing spiky Ni particles showed a large resistive switching. The new findings reported in this work, reveal Ni/rGO nanocomposite as an auspicious material for nanoelectronics (functional Schottky contact, n-p heterojunctions) and lithium-ion battery (anode material) applications. We propose a remarkable benefit of the Pt-NiO-Ni-NiO-rGO interface as a part of embedded electronic circuit where a variation of conductivity from metallic to those characteristics of a Schottky contact or a p-n heterojunction is needed.

2. Materials and methods

2.1 Materials

Graphite (powder, <45 μm, ≥ 99.99%, Sigma-Aldrich), Diethylene glycol (≥99.0%, Sigma-Aldrich) and Nickel (II) acetate tetrahydrate (99.999%-Ni, Stream Chemicals) were purchased and used as received.

2.2 Synthesis of graphene oxide

GO was obtained from graphite using the modified Hummers method, which consists in the exfoliation of graphite into individual GO layers via oxidative process.[5] Briefly, 2 g of graphite was dispersed in 50 mL of sulfuric acid, after that 7 g of potassium permanganate was added slowly to the reaction medium and kept aging for 2 hours. The reaction was stopped by addition of H_2O_2 (30 wt % in water). The resultant suspension was intensively washed with distilled water by filtration until solution reached the neutral pH. Finally, GO solution was lyophilized and a dried powder was obtained.

2.3 Solvothermal synthesis of nickel/graphene oxide nanocomposites (Ni/GO)

For the synthesis of Ni/GO nanocomposites, 2 mg of Ni (II) acetate was firstly dissolved in 10 mL of diethylene glycol (DEG) by 3h mechanical stirring. After that, 10 mg of GO was added to the solution and sonicated during 15 minutes in order to obtain a homogeneous brownish GO dispersion. The mixture was transferred to a 25 mL Teflon autoclave and heated at 150 °C for 1, 3, 6 and 24 hours. The resultant samples were labelled as Ni/GO1, Ni/GO3 and Ni/GO6 and Ni/GO24, respectively (Table 1). After cooling down, the samples were subjected to centrifugal separation and then washed extensively with deionized water and finally freeze-dried.

2.4. Thermal annealing of nanocomposites under hydrogen atmosphere (Ni/rGO)

All the samples prepared by solvothermal method were heat treated in a tubular furnace at 450 °C with the rate of 5 °C/min, under H_2 flow of 8 mL/min during 2 h. The obtained samples were labelled as Ni/rGO1, Ni/rGO3, Ni/rGO6 and Ni/rGO24, respectively (Table 1).

Table 1. Ni/GO nanocomposites prepared by two-step methodology: solvothermal synthesis followed by thermal annealing (hydrogen atmosphere at 450 °C during 2h). The different Ni/GO nanocomposites obtained by different solvothermal reaction times are directly correlated with the respective final electrical properties.

Nickel/reduced graphene oxide nanocomposites							
Solvothermal synthesis (1st step)			**Thermal annealing under H_2/450 °C (2nd step)**				
Sample	***Reaction time (h)***	***XRD***	***Sample***	***XRD***	***Particle size (nm)***	***[Ni] %m/m ICP***	***Electrical properties C-AFM***
Ni/GO1	1	Amorphous Ni	Ni/rGO1	metallic Ni / NiO	5.9±3.2	8.0	metallic contact
Ni/GO3	3		Ni/rGO3		4.4±2.6	3.0	Schottky/partly metallic contact
Ni/GO6	6		Ni/rGO6		8.7±4.0	2.8	Schottky contact
Ni/GO24	24		Ni/rGO24		10.5±3.8	2.8	n-p heterojunction

2.5. Materials Characterization

The powder X-ray diffraction (XRD) patterns of the samples were collected at room temperature in a continuous scanning mode (step 0.04°) using a powder diffractometer PANalytical Empyrean with a secondary monochromator CuKα radiation in the range of $5° \leq 2\theta \leq 90°$. The Raman spectra were collected using a Thermo Scientific DXR smart

Raman Spectrometer with excitation wavelength of 532 nm with a power of 10 mW. Transmission electron microscope (TEM) and high resolution TEM (HRTEM) images were taken with a FEI Tecnai G2 20 and a FEI Titan3 80-300 microscope. Fourier-transform infrared spectroscopy (FTIR) data were collected from KBr pellets using a FTIR Bruker Tensor 27 with the resolution of 4 cm^{-1} in the range of 500-4000 cm^{-1}. X-ray photoelectron spectroscopy (XPS) was carried out in a system equipped with a SPECS Phoibos 150 and monochromatic Al Kα X-ray source. The spectra were recorded at normal emission take-off angle and with a pass-energy of 20 eV. XPS data in this study were calibrated for BE C1s = 284.5 eV.[25] Inductively coupled plasma optical emission spectroscopy (ICP-OES) technique was used to determine the Ni content in each synthesized nanocomposite. This measurement was carried out using an ICP-OES, Horiba Jobin-Yvon, Activa M model with forward power of 1000W, 12 L/min argon flow plasma and sheath gas 0.8 L/min equipped with a Burgener MiraMist nebulizer.

Nanoscale characterization of the samples was carried out by using a commercial scanning probe microscope NTEGRA Prima (NT-MDT) operating in semicontact and contact Atomic Force Microscopy (AFM), Kelvin Probe Force Microscopy (KPFM), Spreading Resistance (SR) and Conductive Atomic Force Microscopy (c-AFM) modes permitting the topography, surface potential distribution, conductivity and local current measurements to be carried out. Pt-coated NSG03/Pt cantilevers with a resonance frequency of 100 kHz and a force constant of 4 N/m were used. KPFM technique [22] allowed to measure a work function (WF) difference between the tip and the sample according to the equation,

$$V_{CPD} = \frac{W_{tip} - W_{sample}}{-e}$$

where W_{tip} is the WF of the SPM tip, W_{sample} is the WF of the sample, e is the elementary charge, and VCPD is the measured contact potential difference, viz. the surface potential.

The *AC* voltage of the second pass was 0.1 V, the lift height was 50 nm. The bias voltage applied to the samples during the SR and c-AFM measurements varied in the range of 0.1-10 Volts. All the SPM measurements were performed under ambient conditions at the humidity of about 30%.

3. Results and Discussion

3.1 Synthesis and characterization of Ni/rGO nanocomposites

The synthesis of Ni/GO nanocomposites was performed by solvothermal method using DEG as both solvent and reducing agent. The structural analysis of as-prepared nanocomposites (Ni/GO) suggests that Ni species at GO surface are in amorphous state (Table 1/Fig S1a)). FTIR and XPS analysis of Ni/GO nanocomposites showed that the GO underwent reduction process with the increase of reaction time (Fig. S1, S2, S3 and S4 in SI). Besides, high resolution detailed spectra of Ni2p for Ni/GO samples showed the appearance of two major peaks centered at 872.9 and 855.8 eV that can be assigned to $Ni(OH)_2$ phase (Fig. S2). In fact, it was already reported that the use of DEG at a reaction temperature near its boiling point (244 °C) is needed to promote a higher reduction reaction rate and crystallinity of NPs.[26]

After the solvothermal reaction, the formation of crystalline metallic Ni NPs in nanocomposite materials (Ni/rGO) was induced by thermal annealing under H_2 reducing atmosphere (Table 1).The XRD pattern of Ni/rGO nanocomposites (Fig. 1a)) showed three main peaks at 44.4°, 52.0° and 78.0° that can be assigned to (1 1 1), (2 0 0) and (2 2 0) crystal planes of Ni with fcc crystal structure (JCPDS, no. 04-0850). The appearance of a shoulder at 43.0° can be attributed to the (2 0 0) crystal plane of NiO (JCPDS, no. 47-1049). These data suggest that the Ni NPs are composed of a core of metallic Ni and a shell of NiO as recently reported by Wang et al.[27] Although, this peak at 43° can be

also attributed to rGO re-staking during the synthesis process of nanocomposites.[28] The peak at 25.0° can be assigned to (0 0 2) rGO layers with the interplanar spacing of 3.52 Å.[29] A slight shift of this peak to the higher 2θ values was observed after thermal annealing under H_2 (see Fig. S1a)), suggesting the effective reduction of GO.[30]

FTIR data (Fig. 1b)) showed the significant reduction of oxygen functional groups in particular for sample Ni/rGO1 and Ni/rGO3, when compared with the data obtained from FTIR after the solvothermal synthesis (Fig. S1b). Nevertheless, it was observed that some oxygen functional groups, such as C-OH (3420 cm^{-1}), C=O (1740 cm^{-1}), C-O (1270 cm^{-1}), C-O-C (1050 cm^{-1}) are retained on rGO even after thermal annealing under H_2. Furthermore, an increase of the intensity of the bands corresponding to CH_2 asymmetric stretching at 2920 cm^{-1} and symmetric stretching at 2850 cm^{-1} was observed, that can be attributed to the restructuration of the graphitic structure.[31]

High resolution XPS spectra of C1s and Ni2p are shown in Fig. 1 (c, d). C1s spectra present a similar profile for all samples (as expected, since they were treated under the same annealing conditions (Table 1)), corresponding to a significant reduction of oxygen functional groups in GO structure (when compared with the GO after solvothermal reaction (Fig. S2)). The small shoulder observed at 286 eV reflects the presence of residual oxygen groups on graphene planes. The high resolution Ni2p spectra (Fig. 1 (d)) exhibits a main peak at 855 eV and a shoulder at 853 eV, that corresponds to the presence of NiO and metallic Ni, respectively. These results evidences that the surface of Ni NPs is in a oxidized state (NiO).[29] The HR-XPS of samples Ni/rGO6 and 24 after Ar+ ion sputtering clearly reveal the presence of metallic nickel (Fig. S3).

Figure 2 (a-d) shows the TEM images of Ni/rGO samples with respective Ni NPs size distribution analysis. Ni NPs reveals a quite similar size distribution for samples Ni/rGO1 (5.9 ± 3.2 nm), Ni/rGO3 (4.4 ± 2.6 nm) and a significant increase of Ni NPs size for

samples Ni/rGO6 (8.7 ± 4 nm) and Ni/rGO24 (10.50 ± 3.8) (inset in Fig. 2). The topography of Ni/rGO nanocomposites was further investigated by AFM. The obtained results showed the homogeneously distribution and an increase of Ni NPs size on rGO surface with the increase of the solvothermal reaction time (Fig. S5). Besides, this data revealed that the reaction time of the solvothermal synthesis plays an important role in the nucleation and growth of Ni nanoclusters on rGO surface.

3.2 Mechanism of Ni NPs growth on GO during the solvothermal synthesis

The mechanism for the solvothermal synthesis of Ni/GO nanocomposites can be explained by three distinct reaction stages (Fig. 2), based on the data obtained by TEM and XPS. We predict that the first stage involves the heterogeneous nucleation and anchorage of Ni species at GO surface due to the strong interactions with the oxygen functional groups.[5] At this stage the surface of GO is completely saturated by Ni nanoclusters due to the high, however limited, density of oxygen groups. ICP analysis confirms the highest concentration of Ni (8.0 % m/m) for sample Ni/rGO1.

The second stage is predominantly governed by the diffusion/dissolution of Ni nanoclusters at the surface of GO after 3 h reaction time. By comparing the TEM images Fig 2a) and 2b), it is possible to observe a drastic decrease of Ni NPs density at rGO surface. Besides, ICP analysis provided further support to this finding, by revealing a significant decrease of the concentration of Ni to 3.0%m/m. We suggest that the most resilient oxygen groups and structural defects on GO can provide stronger anchorage sites for the remaining Ni nanoclusters. However, those Ni nanoclusters that nucleate on minor resilient oxygen groups (for example, epoxides) can be easily detached during the reduction process of GO.[32] XPS data showed the occurrence of a strong reduction of GO for solvothermal reaction time 3h (Fig. S2). These results give clear evidences of the

correlation between the degree of reduction of GO and the decrease of the concentration of Ni on Ni/GO nanocomposites over the reaction time.

The third stage, that occurs for 6 and 24h of solvothermal reaction time, is mainly governed by the coalescence of neighboring Ni nanoclusters for the growth into nanoparticles with larger sizes. This phenomenon can explain the decrease of the density of primary Ni nanoclusters and continuous growth of Ni NPs at the surface of rGO with increasing of solvothermal reaction time observed by TEM (Fig. 2 c) and d)) and AFM (Fig. S5). Moreover, the ICP results showed that the concentration of Ni is constant (2.8 %m/m) for samples prepared with solvothermal reaction time 6h (Ni/GO6) and 24h (Ni/GO24).

3.3 Structural analysis of interface NiO/Ni/rGO of the nanocomposites

HRTEM analysis of nanocomposite Ni/rGO1 reveals the formation of random oriented Ni NPs with spherical morphology (Fig. 3 a and b). In addition, the image shows that Ni nanoparticles are fully embedded on the rGO matrix (Fig. 3a). A magnified close-up of a selected area showed that lattice fringes of NPs present an interplanar distance of approximately 0.24 nm, corresponding to the NiO (111) crystal planes (Fig. 3b).[29] The surface oxidation of Ni nanoparticles was also detected by XPS analysis, which confirms the formation of core-shell Ni/NiO structure of NPs,[24] even after thermal treatment at 450 °C under H_2 atmosphere.

With the purpose of further understanding the atomic structure of the Ni/rGO nanocomposites, electron energy-loss spectroscopy (EELS) analysis was conducted (Fig. 4). The peaks of the O-K edge (~532 eV) and Ni-L2,3 edges (~854 eV) indicate the presence of oxygen and nickel atoms, respectively (Fig. 4(b)).[33] Chemical mapping of the O-K and the Ni-L edge EEL spectra show the distribution of O (yellow), and Ni (red) with sub-nm spatial resolution (Fig. 4 (c)).[34] The obtained results showed the formation

of a core-shell like structure with a shell of O and inner core of metallic Ni. Furthermore, the different gradient of the contrast from the center to the border of Ni NPs shows a non-uniform cover layer of NiO, being more intense on the boundaries between Ni NPs and rGO.

3.4 Local electrophysical measurements of Ni/rGO nanocomposites

Kelvin Probe Force Microscopy (KPFM) carried out for the reference rGO sample shows a homogeneous potential distribution corresponding to the work function of ~ 4.7 ± 0.4 eV (Fig. 5(a)). The value is consistent with the previously reported data (Table 2).

Table 2. Recommended work functions for polycrystalline materials.[35]

Material(polycrystalline)	Work function, eV
Pt	5.5 ± 0.4
Graphite	4.6±0.3
rGO	4.3±0.2
Ni	5.2±0.2
NiO	5.8±0.2

KPFM responses measured on the surface of the Ni/rGO nanocomposites suggest a distribution of the electric potential. The Ni NPs appeared as dark dots with a lower VCPD signal (higher WF) as compared to the rGO matrix (Fig. 5). Being measured at the very local scale (~2 x 2 μm), the sample Ni/rGO1 demonstrates a uniform KPFM response (Fig. 5(b)). For the 1h sample, this kind of behavior could be linked with an effect of doping of the rGO matrix with Ni ions without formation of the NPs and/or nanoclusters. On the contrary, the samples Ni/rGO3, Ni/rGO6 and Ni/rGO24 show a random distribution of the NPs at the local scale (Fig. 5(c-e)). The results correlate well with the TEM data (Fig. 2), even though the size of the particles cannot be determined precisely due to the large tip apex radius (~ 25 nm) and huge impact of electrostatic interaction

between the tip and Ni/rGO composite surface. It has been pointed out that increasing the reaction time (from 1 to 24 hours) gives rise to increase of both the Ni NPs size and NiO layer thickness. The latter plays an important role in the interaction between the Ni NPs via changing the electrostatic force from attractive to repulsive.[24] This assumption is fully consistent with the VCPD values (Fig. 5(b-e)) decreasing with an increase of the Ni NPs diameter and NiO layer width.

The Ni/rGO3 and Ni/rGO6 samples show similar KPFM responses from the Ni NPs distributed in the rGO matrix (Fig. 5(c) and (d)). However, the difference in reaction time causes the variation in distribution of Ni NPs (Ni/rGO3 sample exhibits a more pronounced trend towards the formation of NPs agglomerations). It is interesting to note that an additional KPFM phase (appeared as a strong background) corresponding to the work function of graphene was measured in these samples (the effect is most clearly seen in Ni/rGO6 nanocomposite). The pattern of this background is close to that characterizing the NPs distribution. We suppose that one of the possible reasons underlying the appearance of such a background could be the formation of graphene NPs during the heating (annealing) of rGO matrix accompanying the Ni/rGO3 and Ni/rGO6 samples fabrication. Additional KPFM measurements performed at different second pass heights (10-100 nm) and integral current amplifying (0.1-1.0 nA) confirm the dissimilar nature of the Ni and background NP signals. In contrast, the Ni/rGO24 sample shows a clear distribution of the individual Ni NPs with lower density due to the change of electrostatic forces to the repulsive (the size of the NPs shown in Fig. 5(e) correlates with the TEM data presented in Fig. 2).

The variation in the VCPD (WF) of the nanocomposites should be associated with a difference in the NiO oxide shell width. The crucial role of the buffering NiO shell in electro-physical behavior of Ni/rGO nanocomposite has been shown in our previous

work.[18] These results have suggested that the increase in the radius of Ni NPs causes the increase in the NiO layer width, thus changing the conductivity of the Ni NPs in the rGO matrix and tuning the dielectric permittivity of the Ni/rGO nanocomposites. Recently, the same behavior has been predicted in the theoretical work of Cheng et al [23] devoted to the calculation of Schottky Barrier Height (SBH) and Schottky-Mott (S-M) limit of the interface between graphene, Ni and NiO layers. The reported values for SBH and S-M were -0.414 eV and -1.023 eV, respectively. The positive charge doping in NiO layer was predicted to take place over the depth of about 1.2 A, which is consistent with the 0.609 eV difference between SBH and S-M. The latter fully correlates with the KPFM data obtained for the Ni/rGO composites (Fig. 5(b-e)).

The Spreading Resistance (SR) measurements were carried out for real mapping of conductivity of different samples, see Fig. S6 and related discussions. These data completely reaffirm a huge impact of Ni NPs on conductivity of the rGO matrix.

The c-AFM measurements were done at the most conductive parts of the Ni/rGO nanocomposites and the reference (rGO) sample (Fig. 6(a) compares the currents registered at ± 3 V). The current–voltage dependence obtained for the rGO sample shows a standard nonlinear p-type semiconductor behavior (Fig. 6(b)). The I–V dependence of the Ni/rGO1 sample demonstrates a typical Ohmic behavior with two distinct regions: 0 ± 25 nA (0 ± 0.05 V) and ± 25 nA ± 50 nA (± 0.05 V ± 3 V), respectively. In this measurement, the microscope apparatus saturation current was achieved at ± 3 V (50 nA). This type of I–V curve is associated with a metallic conductivity of doped rGO matrix.[36] The staircase current-voltage behavior is explained by the Coulomb blockade effect describing by the cooperative quantum tunneling of electrons across Ni NPs.

The forward and backward current-voltage dependences obtained for the Ni/rGO (3, 6, 24) nanocomposites show an obvious diode-like rectifying I–V characteristic (Fig. 6 (d-

f)). It can be seen that during the measuring cycle the diodes polarity can be switched in the range of 0.5-4 V. Based on the analysis of the I-V curve (Fig. 6), the switchable diode behavior in the Ni/rGO (3, 6, 24) samples can be explained by the interaction between Ni NPs, NiO shell and rGO matrix and modulation of diode barriers at both bottom and top (cantilever's tip) electrodes. In particular, the Ni/rGO3 sample demonstrates the Ohmic behavior for the backward pass (Fig. 6(d)), which probably reflects some residual metallic coupling between Ni NPs. The increase in the NiO width causes the typical Schottky-like I–V behavior in the Ni/rGO6 sample (Fig. 6(e)) and schematized in Fig. 7) and n-p heterojunction behavior in the Ni/rGO24 sample (Fig. 6(f)) and schematized in Fig. 7).

In terms of the n-p heterojunction, the Pt-NiO interface plays a role of n-type area and the rGO-NiO interface plays a role of p-type area. Both, the n-type and p-type areas are connected via the Ni NP: *Pt-NiO-Ni-NiO-rGO* (Fig. 7). These results support the theoretical predictions recently reported by Cheng et al.[23] Moreover, our assumption is consistent with the KPFM measurements of the Ni/rGO nanocomposites showing that the broadening of the NiO shell causes the increase of the work function (Fig. 5(b-e)) and decrease of the conductivity (Fig. 6(a)).

4. Conclusions

In summary, we reported a new solvothermal method for the controlled synthesis of rGO-based nanocomposites homogeneously decorated with Ni NPs, ranging from nanocluster to fine discrete NPs. The obtained results revealed the direct correlation between the size/density and Ni/NiO nanostructure of NPs and the degree of oxidation of GO template, for the controlled synthesis of different Ni/rGO nanocomposites. The mechanism of Ni NPs growth on GO suggests that at the initial stage of solvothermal reaction (1h) a fast nucleation of Ni nanoclusters at the GO surface occurs. The increase of the solvothermal reaction time (3, 6 and 24h) promoted constant growth into Ni NPs

by the coalescence of adjacent nanoclusters, promoting a significant decrease of their density at rGO surface. Moreover, it was reported that the thickness of NiO shell increases with the reaction time, even after the thermal treatment at 450 °C in hydrogen atmosphere. The potential advantage of the proposed method is the simple design of different Ni/rGO nanostructured composites, exhibiting tunable electronic functionalities. As it is shown by electrophysical measurements, the work function and conductivity are directly dependent on the Ni NPs radius, NiO buffer layer width and Ni NPs density. This allows to manipulate the conductivity of Pt-NiO-Ni-NiO-rGO interface from metallic with quantum Coulomb blockade effect (Ni/rGO1) to Schottky- (Ni/rGO6) and n-p heterojunction-type (Ni/rGO24) making the prepared Ni/rGO nanocomposite a promising material for micro-, nano- and optoelectronics applications as well as for energy storage technologies.

Acknowledgements

We would like to thank Dr. Alexander Surrey from IFW institute for TEM and HRTEM characterizations. This work was supported by Fundação para a Ciência e Tecnologia (FCT) through the PhD (SFRH/BD/98337/2013) grant of M. Salimian. M. S. Ivanov is grateful to FCT financial support through the project MATIS (CENTRO-01-0145-FEDER-000014) and access to TAIL-UC facility funded under QREN-Mais Centro project ICT_2009_02_012_1890. V. A. Khomchenko and P. A. A. P. Marques are grateful to FCT for financial support through the FCT Investigator Programme (projects IF/00819/2014/CP1223/CT0011 and IF/00917/2013/CP1162/CT0016, respectively). Gil Gonçalves thanks to the Programme: Stimulus of Scientific Employment – Individual Support (CEECIND/01913/2017). We also acknowledge UID/EMS/00481/2019-FCT and CENTRO-01-0145-FEDER-022083 - Centro Portugal Regional Operational

Programme (Centro2020), under the PORTUGAL 2020 Partnership Agreement, through the European Regional Development Fund (ERDF).

Figure captions

Figure 1. XRD patterns (a), FTIR spectra (b), high resolution XPS of C 1s (c) and Ni 2p (d) for different Ni/rGO nanocomposites after thermal treatment under hydrogen at 450 °C during 2 h.

Figure 2. TEM images of the Ni/rGO nanocomposites after reduction under hydrogen atmosphere at 450 °C during 2h (Ni/rGO1 (a), Ni/rGO3 (b), Ni/rGO6 (c), and Ni/rGO24 (d)). Schematic representation of nucleation and growth of Ni NPs at GO surface (not to scale) during 1h, h, 6h, and 24h solvothermal treatment.

Figure 3. a) HRTEM image of Ni/NiO nanoparticle with (b) Fast Fourier transform (FFT) and inverse Fast Fourier transform (IFFT) images of the selected area.

Figure 4 High angle annular dark field (HAADF) image of the nanocomposite Ni/rGO1 (a). EEL spectra corresponding to the marked green area (b). EELS maps of Ni (Ni-L2,3) and O (O-K) and their overlay (merged) (c).

Figure 5. Topography (left) and corresponding KPFM response (right) for reference rGO sample (a); the KPFM responses for Ni/rGO1 (b), Ni/rGO3 (c), Ni/rGO6 (d), and Ni/rGO24 (e) nanocomposites.

Figure 6. A comparison of the currents registered in Ni/rGO and rGO samples at ± 3 V (a); current-voltage behavior of rGO (b), Ni/rGO1 (c), Ni/rGO3 (d), Ni/rGO6 (e), and Ni/rGO24 (f).

Figure 7. The schematic view of the energy diagram for Ni/rGO nanocomposites and the effect caused by the NiO buffer layer.

References

[1] A.T. Didеikin, A.Y. Vul', Graphene Oxide and Derivatives: The Place in Graphene Family, Frontiers in Physics, 6 (2019). https://doi.org/10.3389/fphy.2018.00149

[2] N. Selvakumar, A. Biswas, S.B. Krupanidhi, H.C. Barshilia, Enhanced optical absorption of graphene-based heat mirror with tunable spectral selectivity, Sol. Energy Mater. and Sol. Cells, 186 (2018) 149-153. https://doi.org/10.1016/j.solmat.2018.06.041

[3] M. Khan, M.N. Tahir, S.F. Adil, H.U. Khan, M.R.H. Siddiqui, A.A. Al-warthan, W. Tremel, Graphene based metal and metal oxide nanocomposites: synthesis, properties and their applications, J. Mater. Chem. A, 3 (2015) 18753-18808. https://doi.org/10.1039/C5TA02240A

[4] M. Vaqueiro-Contreras, C. Bartlam, R.S. Bonilla, V.P. Markevich, M.P. Halsall, A. Vijayaraghavan, A.R. Peaker, Graphene oxide films for field effect surface passivation of silicon for solar cells, Sol. Energy Mater. and Sol. Cells, 187 (2018) 189-193. https://doi.org/10.1016/j.solmat.2018.08.002

[5] G. Goncalves, P.A.A.P. Marques, C.M. Granadeiro, H.I.S. Nogueira, M.K. Singh, J. Grácio, Surface Modification of Graphene Nanosheets with Gold Nanoparticles: The Role of Oxygen Moieties at Graphene Surface on Gold Nucleation and Growth, Chem. Mater., 21 (2009) 4796-4802. https://doi.org/10.1021/cm901052s

[6] C. Chen, W. Cai, M. Long, B. Zhou, Y. Wu, D. Wu, Y. Feng, Synthesis of Visible-Light Responsive Graphene Oxide/TiO2 Composites with p/n Heterojunction, ACS Nano, 4 (2010) 6425-6432. https://doi.org/10.1021/nn102130m

[7] K. Yang, L. Feng, X. Shi, Z. Liu, Nano-graphene in biomedicine: theranostic applications, Chem. Soc. Rev., 42 (2013) 530-547. https://doi.org/10.1039/C2CS35342C

[8] F. Li, X. Jiang, J. Zhao, S. Zhang, Graphene oxide: A promising nanomaterial for energy and environmental applications, Nano Energy, 16 (2015) 488-515. https://doi.org/10.1016/j.nanoen.2015.07.014

[9] L. Shang, T. Bian, B. Zhang, D. Zhang, L.-Z. Wu, C.-H. Tung, Y. Yin, T. Zhang, Graphene-Supported Ultrafine Metal Nanoparticles Encapsulated by Mesoporous Silica: Robust Catalysts for Oxidation and Reduction Reactions, Angew. Chem. Int. Ed., 53 (2014) 250-254. https://doi.org/10.1002/anie.201306863

[10] I.V. Lightcap, T.H. Kosel, P.V. Kamat, Anchoring Semiconductor and Metal Nanoparticles on a Two-Dimensional Catalyst Mat. Storing and Shuttling Electrons with Reduced Graphene Oxide, Nano Letters, 10 (2010) 577-583. https://doi.org/10.1021/nl9035109

[11] D.-H. Chen, C.-H. Hsieh, Synthesis of nickel nanoparticles in aqueous cationic surfactant solutions, J. Mater. Chem., 12 (2002) 2412-2415. https://doi.org/10.1039/B200603K

[12] Y. Chen, Y. Guo, S. Batra, E. Wang, Y. Wang, X. Liu, Y. Wang, M. Cakmak, Transparent and through thickness conductive polystyrene films using external magnetic fields for "Z" alignment of nickel nanoparticles, Nanoscale, 7 (2015) 14636-14642. https://doi.org/10.1039/C5NR03328D

[13] J. Yang, Z. Qiu, C. Zhao, W. Wei, W. Chen, Z. Li, Y. Qu, J. Dong, J. Luo, Z. Li, Y. Wu, In Situ Thermal Atomization To Convert Supported Nickel Nanoparticles into Surface-Bound Nickel Single-Atom Catalysts, Angew. Chem. Int. Ed., 57 (2018) 14095-14100. https://doi.org/10.1002/anie.201808049

[14] C. Zhou, J.A. Szpunar, X. Cui, Synthesis of Ni/Graphene Nanocomposite for Hydrogen Storage, ACS Appl. Mater. Interfaces, 8 (2016) 15232-15241. https://doi.org/10.1021/acsami.6b02607

[15] Y. Liu, C. Gao, Q. Li, H. Pang, Nickel Oxide/Graphene Composites: Synthesis and Applications, Chem.: Eur. J., 25 (2019) 2141-2160. 10.1002/chem.201803982

[16] Y. Tian, Y. Liu, F. Pang, F. Wang, X. Zhang, Green synthesis of nanostructed Ni-reduced graphene oxide hybrids and their application for catalytic reduction of 4-nitrophenol, Colloids and Surf. A Physicochem. Eng. Asp., 464 (2015) 96-103. https://doi.org/10.1016/j.colsurfa.2014.10.027

[17] N. Li, M. Cao, C. Hu, A simple approach to spherical nickel-carbon monoliths as light-weight microwave absorbers, J. Mater. Chem., 22 (2012) 18426-18432. 10.1039/C2JM32853D

[18] B. Zhang, Y. Wang, X. Dai, D. Liu, X. He, A nitrogen and sulfur co-doped graphene-supported nickel tetrapyridyloxyphthalocyanine hybrid fabricated by a solvothermal method and its application for the detection of bisphenol A, RSC Advances, 5 (2015) 84457-84464. https://doi.org/10.1039/C5RA14516C

[19] W.-C. Wei, C. Deng, S.-C. Huang, Y.-X. Wei, Y.-Z. Wang, Nickel-Schiff base decorated graphene for simultaneously enhancing the electroconductivity, fire resistance, and mechanical properties of a polyurethane elastomer, J. Mater. Chem. A, 6 (2018) 8643-8654. https://doi.org/10.1039/C8TA01287C

[20] K. Zhang, J. Ran, B. Zhu, H. Ju, J. Yu, L. Song, S.-Z. Qiao, Nanoconfined Nickel@Carbon Core–Shell Cocatalyst Promoting Highly Efficient Visible-Light Photocatalytic H2 Production, Small, 14 (2018) 1801705. https://doi.org/10.1002/smll.201801705

[21] H. Yuan, F. Yan, C. Li, C. Zhu, X. Zhang, Y. Chen, Nickel Nanoparticle Encapsulated in Few-Layer Nitrogen-Doped Graphene Supported by Nitrogen-Doped Graphite Sheets as a High-Performance Electromagnetic Wave Absorbing Material, ACS Appl. Mater. Interfaces, 10 (2018) 1399-1407. https://doi.org/10.1021/acsami.7b15559

[22] M. Patange, S. Biswas, Structure dependent magnetic and electrical properties of graphitic carbon encapsulated Ni/NiO core/shell nanoparticles, J. Alloys Comp., 724 (2017) 799-812. https://doi.org/10.1016/j.jallcom.2017.07.015

[23] K. Cheng, N. Han, Y. Su, J. Zhang, J. Zhao, Schottky barrier at graphene/metal oxide interfaces: insight from first-principles calculations, Sci. Rep., 7 (2017) 41771. https://doi.org/10.1038/srep41771

[24] M. Salimian, M. Ivanov, F.L. Deepak, D.Y. Petrovykh, I. Bdikin, M. Ferro, A. Kholkin, E. Titus, G. Goncalves, Synthesis and characterization of reduced graphene oxide/spiky nickel nanocomposite for nanoelectronic applications, J. Mater. Chem. C, 3 (2015) 11516-11523. https://doi.org/10.1039/C5TC02619A

[25] N.I. Kovtyukhova, Y. Wang, A. Berkdemir, R. Cruz-Silva, M. Terrones, V.H. Crespi, T.E. Mallouk, Non-oxidative intercalation and exfoliation of graphite by Brønsted acids, Nat. Chem., 6 (2014) 957. https://doi.org/10.1038/nchem.2054

[26] S. Mourdikoudis, T. Altantzis, L.M. Liz-Marzán, S. Bals, I. Pastoriza-Santos, J. Pérez-Juste, Hydrophilic Pt nanoflowers: synthesis, crystallographic analysis and catalytic performance, Cryst. Eng. Comm., 18 (2016) 3422-3427. https://doi.org/10.1039/C6CE00039H

[27] J. Wang, D. Teschner, Y. Yao, X. Huang, M. Willinger, L. Shao, R. Schlögl, Fabrication of nanoscale NiO/Ni heterostructures as electrocatalysts for efficient methanol oxidation, J. Mater. Chem. A, 5 (2017) 9946-9951. https://doi.org/10.1039/C7TA01982C

[28] N.A. Mohd Zaid, N.H. Idris, Enhanced Capacitance of Hybrid Layered Graphene/Nickel Nanocomposite for Supercapacitors, Sci. Rep., 6 (2016) 32082. https://doi.org/10.1038/srep32082

[29] Y. Si, E.T. Samulski, Exfoliated Graphene Separated by Platinum Nanoparticles, Chem. Mater., 20 (2008) 6792-6797. https://doi.org/10.1021/cm801356a

[30] Y. Chen, Z. Huang, H. Zhang, Y. Chen, Z. Cheng, Y. Zhong, Y. Ye, X. Lei, Synthesis of the graphene/nickel oxide composite and its electrochemical performance for supercapacitors, Int. J. Hydrog Energy, 39 (2014) 16171-16178. https://doi.org/10.1016/j.ijhydene.2014.01.165

[31] Y. Xia, Y. Xiong, B. Lim, S.E. Skrabalak, Shape-Controlled Synthesis of Metal Nanocrystals: Simple Chemistry Meets Complex Physics?, Angew. Chem. Int. Ed., 48 (2009) 60-103. https://doi.org/10.1002/anie.200802248

[32] S. Pei, H.-M. Cheng, The reduction of graphene oxide, Carbon, 50 (2012) 3210-3228. https://doi.org/10.1016/j.carbon.2011.11.010

[33] V.R. Galakhov, A.S. Shkvarin, A.S. Semenova, M.A. Uimin, A.A. Mysik, N.N. Shchegoleva, A.Y. Yermakov, E.Z. Kurmaev, Characterization of Carbon-Encapsulated Nickel and Iron Nanoparticles by Means of X-ray Absorption and Photoelectron Spectroscopy, The J. Phys. Chem. C, 114 (2010) 22413-22416. https://doi.org/10.1021/jp106612b

[34] M. Gong, W. Zhou, M.-C. Tsai, J. Zhou, M. Guan, M.-C. Lin, B. Zhang, Y. Hu, D.-Y. Wang, J. Yang, S.J. Pennycook, B.-J. Hwang, H. Dai, Nanoscale nickel oxide/nickel heterostructures for active hydrogen evolution electrocatalysis, Nat. Commun., 5 (2014) 4695. https://doi.org/10.1038/ncomms5695

[35] D.R. Lide, CRC Handbook of Chemistry and physics, CRC Press, 2005.

[36] W. Park, J. Hu, L.A. Jauregui, X. Ruan, Y.P. Chen, Electrical and thermal conductivities of reduced graphene oxide/polystyrene composites, Appl. Phys. Lett., 104 (2014) 113101. https://doi.org/10.1063/1.4869026

Highlights

- GO showed to be an active substrate for the development of Ni/rGO nanocomposites
- The size and distribution of Ni NPs were tailored by simple control of the solvothermal reaction time
- The NiO@Ni NPs embedded in rGO surface are stable at environmental conditions
- The electrophysical properties were dependent on the Ni NPs radius and NiO shell
- The conductivity of Ni/rGO changed from metallic to a p-n heterojunction.